

# 1 **A new parameterization scheme of the real part of the ambient aerosols refractive index**

2 Gang Zhao<sup>1</sup>, Tianyi Tan<sup>2</sup>, Weilun Zhao<sup>1</sup>, Song Guo<sup>2</sup>, Ping Tian<sup>3</sup>, Chunsheng Zhao<sup>1\*</sup>

3 1 Department of Atmospheric and Oceanic Sciences, School of Physics, Peking University, Beijing,  
4 China

5 2 State Key Joint Laboratory of Environmental Simulation and Pollution Control, College of  
6 Environmental Sciences and Engineering, Peking University, Beijing 100871, China

7 3 Beijing Key Laboratory of Cloud, Precipitation and Atmospheric Water Resources, Beijing 100089,  
8 China

9 **\*Correspondence to: Chunsheng Zhao (zcs@pku.edu.cn)**

## 10 **Abstract**

11 The refractive index of ambient aerosols, which directly determines the aerosol optical properties,  
12 is widely used in atmospheric models and remote sensing. Traditionally, the real part of the refractive  
13 index (RRI) is mainly parameterized by the measurement of ambient aerosol main inorganic  
14 components. In this paper, the characteristics of the ambient aerosol RRI are studied based on the field  
15 measurement in the East China. Results show that the ambient aerosol RRI varies significantly between  
16 1.36 and 1.56. The direct aerosol radiative forcing is estimated to vary by 40% corresponding to the  
17 variation of the measured aerosol RRI. We find that the ambient aerosol RRI is highly related with the  
18 aerosol effective density ( $\rho_{\text{eff}}$ ) rather than the main chemical components. However, parameterization  
19 schemes of the ambient aerosol RRI by  $\rho_{\text{eff}}$  are not available due to the lack of corresponding  
20 simultaneous field measurements. For the first time, the size-resolved ambient aerosol RRI and  $\rho_{\text{eff}}$

21 are measured simultaneously by our designed measurement system. A new parameterization scheme  
22 of the ambient aerosols RRI using  $\rho_{eff}$  is proposed. The measured and parameterized RRI agree well  
23 with the correlation coefficient of 0.75 and slope of 0.99. Knowledge of the ambient aerosol RRI would  
24 improve our understanding of the ambient aerosol radiative effects.

## 25 **1 Introduction**

26 Atmospheric aerosols can significantly influence the regional air quality and climate system by  
27 scattering and absorbing the solar radiation (Seinfeld et al., 1998). However, estimation of the aerosol  
28 radiative effects remains large uncertainties due to the high temporal and spatial variations in aerosol  
29 microphysical properties (Levoni et al., 1997). The complex refractive index (RI), which directly  
30 determines the aerosol scattering and absorbing abilities (Bohren and Huffman, 2007), is one of the  
31 most important microphysical parameters of aerosol optics and radiation. RI is widely employed in  
32 atmospheric models and remote sensing (Zhao et al., 2017). When estimating the direct aerosol  
33 radiative forcing (DARF), many studies showed that great uncertainties may arise due to small  
34 uncertainties in the real part of the RI (RRI). It was found that a small perturbation in RRI (0.003) can  
35 lead to an uncertainty of 1% in DARF for non-absorbing particles (Zarzana et al., 2014). An increment  
36 of 12% in the DARF occurred when the RRI increased from 1.4 to 1.5 (Moise et al., 2015) over the  
37 wavelength range between 0.2  $\mu\text{m}$  and 5  $\mu\text{m}$ . Therefore, it is necessary to measure or parameterize the  
38 ambient aerosol RRI with high accuracy.

39 Traditionally, the RRI is derived from measurements of aerosol main inorganic chemical  
40 compositions (Han et al., 2009). For the ambient aerosol with multiple components, linear volume  
41 average of known aerosol chemical composition is widely used to estimate the aerosol effective  
42  $RRI_{eff}$  (Hand and Kreidenweis, 2002; Liu and Daum, 2008; Hänel, 1968; Wex et al., 2002) with :

$$43 \quad RRI_{eff} = \sum_i (f_i \cdot RRI_i) \quad (1)$$

44 Where  $f_i$  and  $RRI_i$  are the volume fraction and real part of refractive index of known composition  
45  $i$ . However, the influences of organic component on the aerosol RRI were not considered when  
46 estimating the RRI using the traditional method. The organic component contributes more than 20%

47 of the total aerosol component in China (Hu et al., 2012; Liu et al., 2014). At the same time, RRI of the  
48 organic aerosol changes significantly between 1.36 and 1.66 (Moise et al., 2015). Ignoring the organic  
49 component may lead to significant biases when estimating the ambient aerosol RRI. The comparison  
50 between the estimated RRI using main aerosol main aerosol composition and measured aerosol RRI  
51 using other method was not available due to the lack of measurement of ambient aerosol RRI.

52 Information of RRI may be helpful for the knowledge of ambient aerosol chemical information.  
53 Many studies find that ambient aerosols of different size have different properties such as shape (Peng  
54 et al., 2016), chemical composition (Hu et al., 2012) and density (Qiao et al., 2018). Up until now,  
55 there is limit information about the size-resolved RRI ( $\widetilde{\text{RRI}}$ ) of ambient particles. Characteristics of the  
56 ambient aerosol  $\widetilde{\text{RRI}}$  were not well studied yet.

57 The RRI of mono-component particle is defined as (Liu and Daum, 2008):

$$58 \quad \frac{\text{RRI}^2 - 1}{\text{RRI}^2 + 2} = \frac{N_A \alpha}{3M} \rho_{\text{eff}} \quad (2)$$

59 where  $N_A$  is the universal Avagadro's number,  $\alpha$  is the mean molecular polarizability,  $M$  is the  
60 molecular weight of the material and  $\rho_{\text{eff}}$  is the mass effective density of the chemical component.  
61 The RRI should be highly related to  $\rho_{\text{eff}}$ . However, there was no study that investigated the  
62 relationship between the RRI and  $\rho_{\text{eff}}$  of ambient aerosol.

63 The  $\rho_{\text{eff}}$  of ambient aerosols is one of the crucial parameters in aerosol thermo-dynamical and  
64 optical models. It can be used to infer the ambient particle aging process (Peng et al., 2016). Based on  
65 equation 2, the aerosol  $\rho_{\text{eff}}$  is directly related to the aerosol RRI. Few studies measure the ambient  
66 aerosol RRI and  $\rho_{\text{eff}}$  simultaneously. So far, parameterizations of the RRI by  $\rho_{\text{eff}}$  using the  
67 simultaneous measurements are not available. Real-time measurements of the  $\rho_{\text{eff}}$  and aerosol RRI  
68 concurrently can help to better understand the relationship between the aerosol RRI and  $\rho_{\text{eff}}$ .

69 In this study, the aerosol  $\widetilde{\text{RRI}}$  and size resolved  $\rho_{\text{eff}}$  ( $\widetilde{\rho}_{\text{eff}}$ ) are measured simultaneously during  
70 a field measurement conducted in Taizhou in the East China. The ambient aerosol  $\widetilde{\text{RRI}}$  is measured  
71 by our designed system, which combines a differential mobility analyzer (DMA) and a single particle  
72 soot photometer (SP2) (Zhao et al., 2018b). The  $\widetilde{\rho}_{\text{eff}}$  is measured by using a centrifugal particle mass  
73 analyzer (CMPA) and a scanning mobility particle sizer (SMPS). The characteristic of the  $\widetilde{\text{RRI}}$  and  
74  $\widetilde{\rho}_{\text{eff}}$  are analyzed in this study. It is the first time that the  $\widetilde{\text{RRI}}$  and  $\widetilde{\rho}_{\text{eff}}$  of the ambient aerosol are

75 measured simultaneously. A parameterization scheme of the RRI by the  $\rho_{\text{eff}}$  using the simultaneous  
76 measurement is proposed. Based on the measured variability of the measured RRI, we estimated the  
77 corresponding variation of the aerosol direct aerosol radiative forcing, which to some extent give  
78 valuable knowledge for the influence of aerosol RRI variations on aerosol radiative effects.

79 The structure of this study is as follows: the descriptions of the instrument setup is given in section  
80 2.1, 2.2 and 2.3. The methodology of evaluating the aerosol optical properties and radiative effects  
81 corresponding to the variations of the measured RRI are shown in section 2.4 and 2.5 respectively.  
82 Section 3.1 describes the characteristics of the measured the  $\widetilde{\text{RRI}}$  and  $\widetilde{\rho}_{\text{eff}}$ . Section 3.3 proposes the  
83 parameterization of the aerosol RRI. The corresponding variations in aerosol optical properties and  
84 radiative effects corresponding to the variations of the measured RRI are both discussed in section 3.4.

## 85 **2 Data and Methods**

### 86 **2.1 Description of the measurement campaign**

87 The measurement was conducted in a suburban site Taizhou (119°57'E, 32°35'N), as shown in  
88 fig. 1(a), which lies in the south end of the Jianghuai Plain in the central Eastern China. It is located  
89 on the north east of the megacity Nanjing with a distance of 118 km. Another megacity Shanghai is  
90 200 km away from Taizhou in the southeastern direction. The industrial area between Nanjing and  
91 Shanghai has experienced severe pollutions in the past twenty years. The average Moderate Resolution  
92 Imaging Spectroradiometer (MODIS) aerosol optical depth data at 550nm over the year 2017, as  
93 shown in fig. 1(b), also reflects that the measurement site is more polluted than the surrounding areas.

94 During the field campaign, all of the instruments were placed in a container, in which the temperature  
95 was well controlled within  $24 \pm 2$  °C. The sample air was collected from a PM<sub>10</sub> impactor (Mesa Labs,  
96 Model SSI2.5) mounted on the top of the container and then passed through a Nafion dryer tube to  
97 ensure that the relative humidity of the sample particles was controlled below 30%.

98 Along with the measurement of the  $\widetilde{\text{RRI}}$  and  $\widetilde{\rho}_{\text{eff}}$ , the aerosol scattering coefficients ( $\sigma_{\text{sca}}$ ) at three  
99 different wavelengths (450, 525 and 635 nm) were measured by an nephelometer (Aurora 3000,  
100 Ecotech, Australia) (Müller et al., 2011) at a resolution of 5 minutes. The scattering truncation and  
101 non-Lambertian error was corrected using the same method as that of Ma et al. (2011). The aerosol

102 water-soluble ions ( $\text{NH}_4^+$ ,  $\text{SO}_4^{2-}$ ,  $\text{NO}_3^-$ ,  $\text{Cl}^-$ ) of  $\text{PM}_{2.5}$  were measured by an In situ Gas and Aerosol  
103 Compositions Monitor (TH-GAC3000, China). The mass concentration of elementary carbon and  
104 organic carbon (OC) were measured using a thermal optical transmittance aerosol carbon analyzer  
105 (ECOC, Focused Photonics Inc.). The concentrations of Organic matters (OM) are achieved through  
106 multiplying OC concentration by 1.4 (Hu et al., 2012). The time resolution of the aerosol composition  
107 measurement was one hour.

## 108 **2.2 Measuring the $\widetilde{\text{RRI}}$**

109 A coupling DMA-SP2 system was employed to measure the aerosol  $\widetilde{\text{RRI}}$  from 24<sup>th</sup>, May to 18<sup>th</sup>,  
110 June in 2018. This system is introduced elsewhere by Zhao et al. (2018b) and a brief description is  
111 presented here. As schematically shown in fig. S1, the monodispersed aerosols selected by a DMA  
112 (Model 3081, TSI, USA) are drawn into a SP2 to measure the corresponding scattering properties. The  
113 SP2 is capable of distinguishing the pure scattering aerosols from the black carbon (BC) containing  
114 aerosols by measuring the incandescence signals at 1064 nm. For the pure scattering aerosol, the  
115 scattering strength (S) measured by SP2 is expressed as:

$$116 \quad S = C \cdot I_0 \cdot (\sigma_{45^\circ} + \sigma_{135^\circ}) \quad (3),$$

117 where  $C$  is a constant that is determined by the instrument response character;  $I_0$  is the instrument's  
118 laser intensity;  $\sigma_{45^\circ}$  and  $\sigma_{135^\circ}$  is the scattering function of the sampled aerosol at  $45^\circ$  and  $135^\circ$ ,  
119 respectively;. From Mie scattering theory, aerosol size and RRI directly determine the scattering  
120 function at a given direction. Inversely, the aerosol RRI can be retrieved when the aerosol size and  
121 scattering strength are determined. This system can measure the ambient aerosol  $\widetilde{\text{RRI}}$  with uncertainty  
122 less than 0.02 (Zhao et al., 2018b).

123 Before the measurement, this system is calibrated with ammonia sulfate (RRI=1.52). The  
124 relationships between the diameter and the measured scattering peak height are shown in fig. S2. After  
125 calibration, ammonium chloride is used to validate the method of deriving the RRI at different aerosol  
126 diameters. The RRI value of ammonium chloride is 1.642 (Lide, 2006) and the measured RRI of  
127 ammonium chloride is in the range between 1.624 and 1.656 in our study. Therefore, this measurement  
128 system can measure the ambient aerosol RRI with high accuracy.

## 129 **2.3 Measuring the $\widetilde{\rho}_{\text{eff}}$**

130 The  $\widetilde{\rho}_{\text{eff}}$  is measured by a Centrifugal Particle Mass Analyzer (CPMA, version 1.53, Cambustion  
131 Ltd, UK) in tandem with a Scanning Mobility Particle Sizer (SMPS) system from 12<sup>th</sup>, June to 18<sup>th</sup>,  
132 June in 2018. The  $\rho_{\text{eff}}$  is defined as

$$133 \quad \rho_{\text{eff}} = \frac{m_p}{\frac{\pi}{6} \times d_m^3} \quad (4),$$

134 Where  $m_p$  is the particle mass and  $d_m$  is the aerosol mobility diameter selected by DMA.

135 The controlling of the CPMA-SMPS system is achieved by self-established Labview software.  
136 The CPMA is set to scan twelve different aerosol mass at 1.0, 1.4, 2.0, 2.9, 4.2, 5.9, 8.5, 12.1, 17.2,  
137 24.6, 35.0 and 50.0 fg every five minutes respectively. The SMPS scan the aerosol diameters between  
138 60nm and 500nm every 5 minute, which results in a period of one hour for measuring the effective  
139 density of different mass.

140 At the beginning of the field measurement, the CPMA-SMPS system is calibrated using the PSL  
141 particles with different mass. The corresponding measured effective densities of PSL particles are 1.04  
142 and 1.07 g/cm<sup>3</sup>, which agree well with the PSL material density of 1.05 g/cm<sup>3</sup>.

#### 143 **2.4 Calculate aerosol optical properties using different RRI**

144 The aerosol optical properties are highly related to the RRI. From Mie scattering theory, the variation  
145 in aerosol RRI may result in significant variations in the aerosol optical properties, such as aerosol  
146 extinction coefficient ( $\sigma_{\text{ext}}$ ), the  $\sigma_{\text{sca}}$ , the single scattering albedo (SSA), and the asymmetry factor  
147 ( $g$ ) (Bohren and Huffman, 2007). SSA is defined as the ratio of  $\sigma_{\text{sca}}$  to  $\sigma_{\text{ext}}$ , which reflects  
148 concentration of the absorbing aerosol (Tao et al., 2014) to some extent. The  $g$  expresses the  
149 distribution of the scattering light intensity in different directions (Zhao et al., 2018a). The  $\sigma_{\text{ext}}$ , SSA  
150 and  $g$  are the most important three factors that influence the aerosol radiative properties in radiative  
151 calculation (Kuang et al., 2015).

152 In this study, the sensitivity studies of the aerosol optical properties to the aerosol RRI are carried  
153 out by employing the Mie scattering theory. The input variables of Mie scattering model includes the  
154 aerosol PNSD and BC mixing state and aerosol complex refractive index. The Mie model can calculate  
155 the  $\sigma_{\text{ext}}$ ,  $\sigma_{\text{sca}}$ , SSA and  $g$ . The mixing state of the ambient BC comes from the measurements of the  
156 DMA-SP2 system. All of the aerosols are divided into pure scattering aerosols and BC-containing  
157 aerosols. The BC-containing aerosols are assumed to be core-shell mixed. As for the RI of BC,

158 1.8+0.54i is used (Kuang et al., 2015). With this, the aerosol  $\sigma_{\text{ext}}$ ,  $\sigma_{\text{sca}}$ , SSA and g at different RRI  
159 values can be calculated.

## 160 2.5 Estimating the aerosol DARF

161 In this study, the DARF under different aerosol RRI conditions is estimated by the Santa Barbara  
162 DISORT (discrete ordinates radiative transfer) Atmospheric Radiative Transfer (SBDART) model  
163 (Ricchiazzi et al., 1998). Under the cloud-free conditions, DARF at the TOA is calculated as the  
164 difference between radiative flux under aerosol-free conditions and aerosol present conditions:

$$165 \text{DARF} = (f_a \downarrow - f_a \uparrow) - (f_n \downarrow - f_n \uparrow) \quad (5),$$

166 where  $f_a \downarrow$  and  $f_a \uparrow$  are the downward and upward radiative irradiance with aerosol present  
167 conditions respectively; the difference between  $f_a \downarrow$  and  $f_a \uparrow$  ( $f_a \downarrow - f_a \uparrow$ ) is the downward radiative  
168 irradiance flux with aerosol present conditions;  $f_n \downarrow$  and  $f_n \uparrow$  correspond to the downward and  
169 upward radiative irradiance values under aerosol free conditions respectively; the difference between  
170  $f_n \downarrow$  and  $f_n \uparrow$  ( $f_n \downarrow - f_n \uparrow$ ) is the downward radiative irradiance flux for aerosol-free conditions  
171 (Kuang et al., 2016). The instant DARF value is calculated over the wavelength range between 0.25  
172  $\mu\text{m}$  and 4  $\mu\text{m}$ .

173 Input data for the model are shown below. The vertical profiles of temperature, pressure and water  
174 vapor, which adopt the radiosonde observations at Taizhou site. The measured mean results  
175 corresponding the field measurement period are used. Vertical distributions of aerosol  $\sigma_{\text{ext}}$ , SSA and  
176 g with a resolution of 50 m, are resulted from the calculation using the Mie Model and parameterized  
177 aerosol vertical distributions. Methods for parameterization and calculation of the aerosol optical  
178 profiles can be found in Sect. S3 or in Zhao et al. (2018a). The surface albedo adopt the mean results  
179 of MODIS V005 Climate Modeling Grid (CMG) Albedo Product (MCD43C3) at the area of Taizhou  
180 from May, 2017 to April, 2018. The other default values are used in the simulation (Ricchiazzi et al.,  
181 1998).

## 182 3 Results and Discussions

### 183 3.1 The Measurements Results

184 The overview of the measurement is shown in fig. 2. During the measurement, the  $\sigma_{\text{sca}}$  is relatively  
185 low with a mean value of  $167 \pm 74 \text{ Mm}^{-1}$ . There were one major pollution episodes occurred based on

186 the  $\sigma_{\text{sca}}$  time series as shown in fig. 2(a). This pollution happens on 13<sup>th</sup>, June and doesn't last long.  
187 The corresponding  $\sigma_{\text{sca}}$  reaches 540  $\text{Mm}^{-1}$ . A moderate polluted condition between 14<sup>th</sup>, June and  
188 15<sup>th</sup>, June is observed. The aerosol PNSD changes substantially with the pollution conditions as  
189 shown in fig. 2(b). The geometric median aerosol diameter changes between 30 nm and 105 nm. The  
190 median diameter tends to be lower when the surrounding is cleaner. Despite the median diameter  
191 reaches 105 nm on 16<sup>th</sup>, June, the surrounding is relative clean due to the low aerosol number  
192 concentration. The  $\widetilde{\text{RRI}}$  and  $\widetilde{\rho_{\text{eff}}}$  vary from 1.34 to 1.54 and the  $\widetilde{\rho_{\text{eff}}}$  ranges between 1.21 to 1.80  
193  $\text{g}/\text{cm}^3$  as shown in fig. 2 (c) and (d). From fig. 2, the measured RRI shows the same variation pattern  
194 with the  $\rho_{\text{eff}}$ . Both the  $\widetilde{\text{RRI}}$  and  $\widetilde{\rho_{\text{eff}}}$  increase with the diameter, which may indicate that the aerosol  
195 chemical composition varies among different aerosol particle size.

196 As for the  $\widetilde{\text{RRI}}$ , the corresponding mean RRI values for aerosol diameter at 200nm, 300nm and  
197 450nm are  $1.425 \pm 0.031$ ,  $1.435 \pm 0.041$ ,  $1.47 \pm 0.059$ . When comparing the probability distribution of the  
198 RRI for different diameter in fig. 3, the RRI is more dispersed when the particle size increases,  
199 implicating that the aerosol compositions become complicated when the aerosol get aged. Fig. 3 (a),  
200 (c) and (e) give diurnal variation of the  $\widetilde{\text{RRI}}$  values at different particle sizes of 200 nm, 300 nm and  
201 450 nm. The RRI shows diurnal cycles for different diameters. They reach the peak at about 15:00 in  
202 the morning and fall to the valley at around 9:00 in the afternoon.

203 The range of the measured RRI (1.34~1.56) is a little wider than the literature values. The past  
204 measurement of the ambient aerosol RRI values varies between 1.4 and 1.6 (Dubovik, 2002; Guyon et  
205 al., 2003; Zhang et al., 2016) over different measurement site. This is the first time that such high  
206 variations in ambient aerosol RRI were observed at one site.

207 The  $\widetilde{\rho_{\text{eff}}}$  shows almost the same diurnal variations as the  $\widetilde{\text{RRI}}$  as shown fig. S5. The diurnal  
208 variations of the  $\widetilde{\rho_{\text{eff}}}$  is more dispersed because the time period of measuring the  $\widetilde{\rho_{\text{eff}}}$  is shorter (7  
209 days) comparing with the time of  $\widetilde{\text{RRI}}$  (28 days). It is evident that the  $\rho_{\text{eff}}$  increased with particle  
210 size. The difference of  $\rho_{\text{eff}}$  among different particle size should be resulted from different  
211 contributions of chemical compositions, especially the OM. Based on the previous measurement of the  
212 size-resolved chemical compositions using a micro orifice uniform deposit impactors (MOUDI), the  
213 mass fraction of OM get decreased with the increment of aerosol diameter (Hu et al., 2012). At the

214 same time, the effective density of OM is lower than the other main inorganic compositions. Thus, the  
215 effective tend to increase with the increment of aerosol diameter.

### 216 **3.2 Aerosol Chemical Composition versus the RRI**

217 From equation (1) and (2), the aerosol RRI can be determined by aerosol chemical composition (Liu  
218 and Daum, 2008). Many studies calculate the RRI using the measurement results of the relative  
219 contributions of aerosol chemical composition (Yue et al., 1994;Hänel, 1968;Guyon et al.,  
220 2003;Stelson, 1990;Wex et al., 2002). However, there is no comparison between the RRI calculated  
221 from chemical composition and real-time measurement until now. In this study, the relationship  
222 between the measured RRI and the mass fraction of each ion components is investigated.

223 As illustrated in fig. 4, the RRI tend to increase with the OM mass fraction ratio, which implies that  
224 the OM may play an important role in aerosol scattering properties. This is in agreement with the  
225 Aldhaif et al. (2018), where the aerosol OM contributes a lot to the ambient aerosol mass  
226 concentrations. The RRI have implicit relationship with the mass fraction of the  $\sigma_{\text{sca}}$  at 525 nm,  
227  $\text{SO}_4^{2-}$ ,  $\text{Cl}^-$ , and  $\text{NO}_3^-$ . The mass ratio of  $\text{NH}_4^+$  seems to be negatively correlated with the RRI. At  
228 the same time, the measured RRI values have no clear relationship with the absolute mass  
229 concentrations of the main aerosol chemical components, as shown in fig. S6.

230 The RRI is also calculated by applying the method proposed by Stelson (1990), in which the bulk  
231 chemical composition is used. The comparison between the calculated RRI and the measured RRI is  
232 shown in fig. 5. It can be noticed that the calculated RRI and the measured RRI doesn't agree well.  
233 There are several reasons that may cause the discrepancies. The first reason might be that the aerosol  
234 chemical information used in the method is the average mass of whole aerosol population. The aerosol  
235 chemical composition may vary significantly among different size. Secondly, the OM of the ambient  
236 aerosols is very complicated and the influence of the OM on the aerosol RRI has not been studied well.  
237 Therefore, more research is necessary when parameterizing the ambient aerosol RRI with the measured  
238 aerosol chemical composition.

### 239 **3.3 Parameterizing the RRI using $\rho_{\text{eff}}$**

240 As shown in fig. 2, there is good consistence between the variation of the measured  $\widetilde{\text{RRI}}$  and  $\widetilde{\rho_{\text{eff}}}$ .

241 When defining the specific refractive index  $\text{Re}$  with  $\text{Re} = \frac{\text{RRI}^2 - 1}{\text{RRI}^2 + 2}$ , we found that the  $\text{Re}$  is highly

242 correlated with  $\rho_{eff}$  by a  $R^2$  equaling 0.75 and slope 0.99 (fig. 5). The linear relationships between  
243 the  $R_e$  and  $\rho_{eff}$  is:

$$244 \quad \frac{RRI^2-1}{RRI^2+2} = 0.18\rho_{eff} \quad (6).$$

245 The RRI can be calculated based on equation 6:

$$246 \quad RRI = \sqrt{\frac{1+0.36\rho_{eff}}{1-0.18\rho_{eff}}} \quad (7).$$

247 Based on equation 7 and fig. 6 the aerosol RRI can be parameterized by the  $\rho_{eff}$  with high accuracy  
248 and the uncertainties of the calculated RRI using equation 7 can be constrained within 0.025. The  
249 aerosol  $\rho_{eff}$  is easier to be measured, and equation 7 might be used as a good probe of parameterizing  
250 the RRI.

251 To demonstrate the universality of this parameterization scheme, we conducted another  
252 measurement in the campus of Peking University (PKU) (N39°59', E116°18'), in North China Plain,  
253 where the aerosol effective density and real part of the refractive index are measured concurrently at  
254 16<sup>th</sup>, December in 2018. The measurement last only one days because some instruments were borrowed  
255 from other institute. The RRI were also calculated using the parameterization scheme equation 7. The  
256 slope and correlation coefficient at PKU site are 1.0 and 0.47 respectively. The calculated and  
257 measured RRI show good consistence. Therefore, this scheme is applicable for different seasons at  
258 both Center China and North China Plain.

259 This parameterization scheme is easy to use because the effective density is the only parameter used  
260 as input. We have demonstrated that the traditional method of calculating the RRI using aerosol main  
261 chemical components can have significant bias because the effects of organic aerosol is not considered.  
262 The RRI can be easy to calculate based on our parameterization scheme, as the effective density of  
263 ambient aerosol is rather easier to measure.

264 In the previous, Liu and Daum (2008) summarized some of the measured RRI and the  $\rho_{eff}$ , and  
265 parameterized the RRI as

$$266 \quad \frac{RRI^2-1}{RRI^2+2} = 0.23\rho^{0.39} \quad (8).$$

267 The feasibility of this scheme is tested here and the results are shown in fig. 5. The measured and  
268 parameterized RRI using the method of Liu and Daum (2008) deviated from 1:1 line. The effective  
269 density and RRI in their work were estimated using the aerosol chemical components but not the field  
270 measurement. At the same time, the influence of organic aerosols components on aerosol RRI is not  
271 considered in their work.

### 272 **3.4 Influence of RRI Variation on Aerosol Optical Properties and Radiative Properties**

273 The measured RRI varies between 1.34 and 1.56 during the field campaign. The corresponding  
274 aerosol optical properties are estimated. When estimating the aerosol optical properties with different  
275 aerosol RRI, the measured mean aerosol PNSD and mixing states are used. Fig. 7 gives the variation  
276 of the aerosol  $\sigma_{\text{sca}}$ , SSA and  $g$ . From fig. 7, the  $\sigma_{\text{sca}}$  varies from  $162 \text{ Mm}^{-1}$  to  $308 \text{ Mm}^{-1}$ . The SSA  
277 varies between 0.843 and 0.895, which matches the variations of the dry aerosol SSA for different  
278 aerosol size distributions in the North China Plain (NCP) (Tao et al., 2014). As for the aerosol  $g$ , it  
279 decreases from 0.667 to 0.602 with the increment of the aerosol RRI. The ambient  $g$  values in the NCP  
280 are found within 0.55 and 0.66 (Zhao et al., 2018a). Thus, the variations of the RRI have significant  
281 influence on the  $g$ . The aerosol optical properties change significantly with the variation of the ambient  
282 aerosol RRI.

283 The instant DARF values under different RRI are also estimated and the results are illustrated in fig.  
284 7(b). When the aerosol RRI increases from 1.4 to 1.5, the DARF varies from -6.17 to -8.35,  
285 corresponding to 15% variation in DARF. This values are in accordance with the work of Moise et al.  
286 (2015), who estimate that an increment of 12% in the DARF occurs when the RRI varies from 1.4 to  
287 1.5. The DARF can change from  $-4.9 \text{ w/m}^2$  to  $-10.14 \text{ w/m}^2$  when the aerosol RRI increase from 1.34  
288 to 1.56, which corresponding to 40% variation in DARF. Great uncertainties may arise when  
289 estimating the aerosol radiative forcing when using a constant RRI. The RRI should be different under  
290 different aerosol conditions. The real time measured RRI should be used rather than a constant RRI  
291 when estimating the ambient aerosol optical and radiative properties. However, the real-time  
292 measurement of ambient aerosol RRI is not available for most of the conditions. Our proposed  
293 parameterizations scheme is a perfect substitute. The only parameter required is aerosol effective  
294 density and it is much easier to measure.

## 295 4 Conclusions

296 The ambient aerosol RRI is a key parameter in determining the aerosol optical properties and  
297 knowledge of it can help constrain the uncertainties in aerosol radiative forcing. In this study, the  
298 ambient aerosol  $\widetilde{RRI}$  were measured at Taizhou, in the Jianghuai Plain of China by using a DMA in  
299 tandem with a SP2 from 24<sup>th</sup>, May to 18<sup>th</sup>, June in 2018.

300 Results show that the ambient aerosol RRI varies over a wide range between 1.34 and 1.56. The  
301 RRI increases slowly with the increment of the aerosol diameter. The mean aerosol RRI values are  
302  $1.425\pm 0.031$ ,  $1.435\pm 0.041$ ,  $1.47\pm 0.059$  for aerosol diameter at 200 nm, 300 nm and 450 nm  
303 respectively. Probability distributions of the RRI show that the RRI is more dispersed with the  
304 increment of aerosol diameter, which reflect the complexing aging processing of the ambient aerosol.  
305 The aerosol optical properties change significantly and the DARF is estimated to vary by 40%  
306 corresponding to the variation of the measured ambient aerosol RRI. The real-time measured RRI  
307 should be used rather than a constant RRI when estimating the ambient aerosol optical and radiative  
308 properties.

309 Traditionally, the ambient aerosol RRI is mainly calculated by using the corresponding measured  
310 main chemical inorganic compositions of aerosols. We find that the ambient aerosol RRI is highly  
311 related with the  $\rho_{eff}$  rather than the main chemical compositions of aerosols. There is discrepancy  
312 between the measured and parameterized RRI using the traditional method. This might be resulted  
313 from two reasons. The first one is that the aerosol chemical information used for calculation is the total  
314 aerosol loading. The aerosol chemical compositions may change significantly among different size.  
315 Another one is that the influence of OM of ambient aerosols is not considered. The RRI of OM varies  
316 significantly for different compositions (Moise et al., 2015).

317 Despite that the RRI is related with the  $\rho_{eff}$ , parameterization scheme of the ambient aerosol RRI  
318 using  $\rho_{eff}$  is not available due to the lack of simultaneously measurement. For the first time, the  $\widetilde{RRI}$   
319 and  $\widetilde{\rho_{eff}}$  were measured simultaneously using our designed system. The  $\widetilde{\rho_{eff}}$  is measured during the  
320 field campaign by employing a CMPA and a SMPS from 12<sup>th</sup>, June to 18<sup>th</sup>, June in 2018.

321 A new parameterization scheme of the ambient aerosol RRI using the  $\rho_{\text{eff}}$  is proposed based on  
322 the field measurement results. The measured and parameterized RRI agree well with the correlation  
323 coefficient of 0.75 and slope of 0.99. This parameterization scheme is validated at another  
324 measurement site at different season. This simple scheme is reliable and ready to be used in the  
325 calculation of aerosol optical and radiative properties. The corresponding measurement results can also  
326 be further used in climate model.

327

328 **Competing interests.** The authors declare that they have no conflict of interest.

329 **Data availability.** The data used in this study is available when requesting the authors.

330 **Author contributions.** GZ, CZ, WZ and SG designed and conducted the experiments; PT, TY and  
331 GZ discussed the results.

332 **Acknowledgments.** This work is supported by the National Natural Science Foundation of China  
333 (41590872) and National Key R&D Program of China (2016YFC020000:Task 5).

## 334 **References**

- 335 Aldhaif, A. M., Stahl, C., Braun, R. A., Moghaddam, M. A., Shingler, T., Crosbie, E., Sawamura, P.,  
336 Dadashazar, H., Ziemba, L., Jimenez, J. L., Campuzano-Jost, P., and Sorooshian, A.: Characterization  
337 of the Real Part of Dry Aerosol Refractive Index Over North America From the Surface to 12 km,  
338 *Journal of Geophysical Research: Atmospheres*, 10.1029/2018jd028504, 2018.
- 339 Bohren, C. F., and Huffman, D. R.: Absorption and Scattering by a Sphere, in: Absorption and  
340 Scattering of Light by Small Particles, Wiley-VCH Verlag GmbH, 82-129, 2007.
- 341 Dubovik, O.: Variability of absorption and optical properties of key aerosol types observed in  
342 worldwide locations, *J.atmos.sci*, 59, 590-608, 2002.
- 343 Guyon, P., Boucher, O., Graham, B., Beck, J., Mayol-Bracero, O. L., Roberts, G. C., Maenhaut, W.,  
344 Artaxo, P., and Andreae, M. O.: Refractive index of aerosol particles over the Amazon tropical forest

345 during LBA-EUSTACH 1999, *Journal of Aerosol Science*, 34, 883-907, 10.1016/s0021-  
346 8502(03)00052-1, 2003.

347 Han, Y., Lü, D., Rao, R., and Wang, Y.: Determination of the complex refractive indices of aerosol  
348 from aerodynamic particle size spectrometer and integrating nephelometer measurements, *Applied*  
349 *Optics*, 48, 4108-4117, 10.1364/AO.48.004108, 2009.

350 Hand, J. L., and Kreidenweis, S. M.: A New Method for Retrieving Particle Refractive Index and  
351 Effective Density from Aerosol Size Distribution Data, *Aerosol Sci. Technol.*, 36, 1012-1026,  
352 10.1080/02786820290092276, 2002.

353 Hänel, G.: REAL PART OF MEAN COMPLEX REFRACTIVE INDEX AND MEAN DENSITY OF  
354 SAMPLES OF ATMOSPHERIC AEROSOL PARTICLES, *Tellus*, 20, 371-&, 371-  
355 10.3402/tellusa.v20i3.10016, 1968.

356 Hu, M., Peng, J., Sun, K., Yue, D., Guo, S., Wiedensohler, A., and Wu, Z.: Estimation of size-resolved  
357 ambient particle density based on the measurement of aerosol number, mass, and chemical size  
358 distributions in the winter in Beijing, *Environ Sci Technol*, 46, 9941-9947, 10.1021/es204073t, 2012.

359 Kuang, Y., Zhao, C. S., Tao, J. C., and Ma, N.: Diurnal variations of aerosol optical properties in the  
360 North China Plain and their influences on the estimates of direct aerosol radiative effect, *Atmos. Chem.*  
361 *Phys.*, 15, 5761-5772, 10.5194/acp-15-5761-2015, 2015.

362 Kuang, Y., Zhao, C. S., Tao, J. C., Bian, Y. X., and Ma, N.: Impact of aerosol hygroscopic growth on  
363 the direct aerosol radiative effect in summer on North China Plain, *Atmospheric Environment*, 147,  
364 224-233, 2016.

365 Levoni, C., Cervino, M., Guzzi, R., and Torricella, F.: Atmospheric aerosol optical properties: a  
366 database of radiative characteristics for different components and classes, *Appl Opt*, 36, 8031-8041,  
367 1997.

368 Lide, D. R.: Handbook of Chemistry and Physics, 86th Edition Edited(National Institute of Standards  
369 and Technology), *Journal of the American Chemical Society*, 128, 5585-5585, 10.1021/ja059868l,  
370 2006.

371 Liu, H. J., Zhao, C. S., Nekat, B., Ma, N., Wiedensohler, A., van Pinxteren, D., Spindler, G., Müller,  
372 K., and Herrmann, H.: Aerosol hygroscopicity derived from size-segregated chemical composition and

373 its parameterization in the North China Plain, *Atmospheric Chemistry and Physics*, 14, 2525-2539,  
374 10.5194/acp-14-2525-2014, 2014.

375 Liu, Y., and Daum, P. H.: Relationship of refractive index to mass density and self-consistency of  
376 mixing rules for multicomponent mixtures like ambient aerosols, *Journal of Aerosol Science*, 39, 974-  
377 986, 10.1016/j.jaerosci.2008.06.006, 2008.

378 Ma, N., Zhao, C. S., Nowak, A., Müller, T., Pfeifer, S., Cheng, Y. F., Deng, Z. Z., Liu, P. F., Xu, W.  
379 Y., Ran, L., Yan, P., Göbel, T., Hallbauer, E., Mildenerger, K., Henning, S., Yu, J., Chen, L. L., Zhou,  
380 X. J., Stratmann, F., and Wiedensohler, A.: Aerosol optical properties in the North China Plain during  
381 HaChi campaign: an in-situ optical closure study, *Atmos. Chem. Phys.*, 11, 5959-5973, 10.5194/acp-  
382 11-5959-2011, 2011.

383 Moise, T., Flores, J. M., and Rudich, Y.: Optical properties of secondary organic aerosols and their  
384 changes by chemical processes, *Chemical Reviews*, 115, 4400-4439, 2015.

385 Müller, T., Laborde, M., Kassell, G., and Wiedensohler, A.: Design and performance of a three-  
386 wavelength LED-based total scatter and backscatter integrating nephelometer, *Atmos. Meas. Tech.*, 4,  
387 1291-1303, 10.5194/amt-4-1291-2011, 2011.

388 Peng, J., Hu, M., Guo, S., Du, Z., Zheng, J., Shang, D., Levy Zamora, M., Zeng, L., Shao, M., Wu, Y.-  
389 S., Zheng, J., Wang, Y., Glen, C. R., Collins, D. R., Molina, M. J., and Zhang, R.: Markedly enhanced  
390 absorption and direct radiative forcing of black carbon under polluted urban environments,  
391 *Proceedings of the National Academy of Sciences*, 113, 4266-4271, 10.1073/pnas.1602310113, 2016.

392 Qiao, K., Wu, Z., Pei, X., Liu, Q., Shang, D., Zheng, J., Du, Z., Zhu, W., Wu, Y., Lou, S., Guo, S.,  
393 Chan, C. K., Pathak, R. K., Hallquist, M., and Hu, M.: Size-resolved effective density of submicron  
394 particles during summertime in the rural atmosphere of Beijing, China, *Journal of Environmental*  
395 *Sciences*, 10.1016/j.jes.2018.01.012, 2018.

396 Ricchiazzi, P., Yang, S., Gautier, C., and Sowle, D.: SBDART: A Research and Teaching Software  
397 Tool for Plane-Parallel Radiative Transfer in the Earth's Atmosphere, *Bulletin of the American*  
398 *Meteorological Society*, 79, 2101-2114, 10.1175/1520-0477(1998)079<2101:sarats>2.0.co;2, 1998.

399 Seinfeld, J. H., Pandis, S. N., and Noone, K.: *Atmospheric Chemistry and Physics: From Air Pollution*  
400 *to Climate Change*, *Environment Science & Policy for Sustainable Development*, 40, 26-26, 1998.

401 Stelson, A. W.: Urban aerosol refractive index prediction by partial molar refraction approach,  
402 *Environ.sci.technol*, 24:11, 1676-1679, 1990.

403 Tao, J. C., Zhao, C. S., Ma, N., and Liu, P. F.: The impact of aerosol hygroscopic growth on the single-  
404 scattering albedo and its application on the NO<sub>2</sub> photolysis rate coefficient, *Atmos. Chem. Phys.*, 14,  
405 12055-12067, 10.5194/acp-14-12055-2014, 2014.

406 Wex, H., Neusüß, C., Wendisch, M., Stratmann, F., Koziar, C., Keil, A., Wiedensohler, A., and Ebert,  
407 M.: Particle scattering, backscattering, and absorption coefficients: An in situ closure and sensitivity  
408 study, *Journal of Geophysical Research: Atmospheres*, 107, LAC 4-1-LAC 4-18,  
409 10.1029/2000jd000234, 2002.

410 Yue, G. K., Poole, L. R., Wang, P. H., and Chiou, E. W.: STRATOSPHERIC AEROSOL ACIDITY,  
411 DENSITY, AND REFRACTIVE-INDEX DEDUCED FROM SAGE-II AND NMC  
412 TEMPERATURE DATA, *J Geophys Res-Atmos*, 99, 3727-3738, 10.1029/93jd02989, 1994.

413 Zarzana, K. J., Cappa, C. D., and Tolbert, M. A.: Sensitivity of Aerosol Refractive Index Retrievals  
414 Using Optical Spectroscopy, *Aerosol Sci. Technol.*, 48, 1133-1144, 10.1080/02786826.2014.963498,  
415 2014.

416 Zhang, G., Bi, X., Qiu, N., Han, B., Lin, Q., Peng, L., Chen, D., Wang, X., Peng, P., apos, an, Sheng,  
417 G., and Zhou, Z.: The real part of the refractive indices and effective densities for chemically  
418 segregated ambient aerosols in Guangzhou measured by a single-particle aerosol mass spectrometer,  
419 *Atmospheric Chemistry and Physics*, 16, 2631-2640, 10.5194/acp-16-2631-2016, 2016.

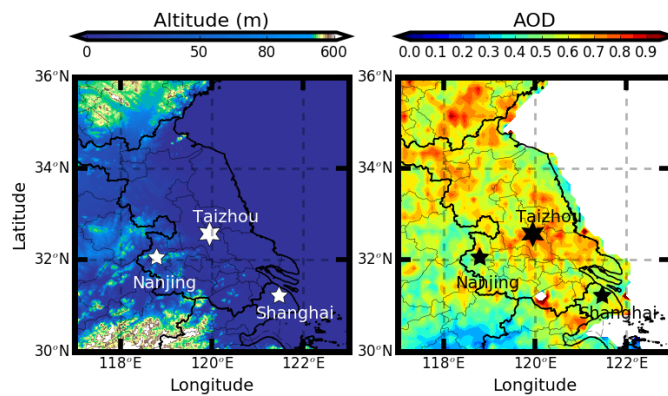
420 Zhao, G., Zhao, C., Kuang, Y., Tao, J., Tan, W., Bian, Y., Li, J., and Li, C.: Impact of aerosol  
421 hygroscopic growth on retrieving aerosol extinction coefficient profiles from elastic-backscatter lidar  
422 signals, *Atmospheric Chemistry and Physics*, 17, 12133-12143, 10.5194/acp-17-12133-2017, 2017.

423 Zhao, G., Zhao, C., Kuang, Y., Bian, Y., Tao, J., Shen, C., and Yu, Y.: Calculating the aerosol  
424 asymmetry factor based on measurements from the humidified nephelometer system, *Atmospheric  
425 Chemistry and Physics*, 18, 9049-9060, 10.5194/acp-18-9049-2018, 2018a.

426 Zhao, G., Zhao, C., Zhao, W., and Hello, W.: Method to measure the size-resolved real part of aerosol  
427 refractive index, *Atmos. Meas. Tech. Discuss.*, 2018, 1-20, 10.5194/amt-2018-399, 2018b.

428

429



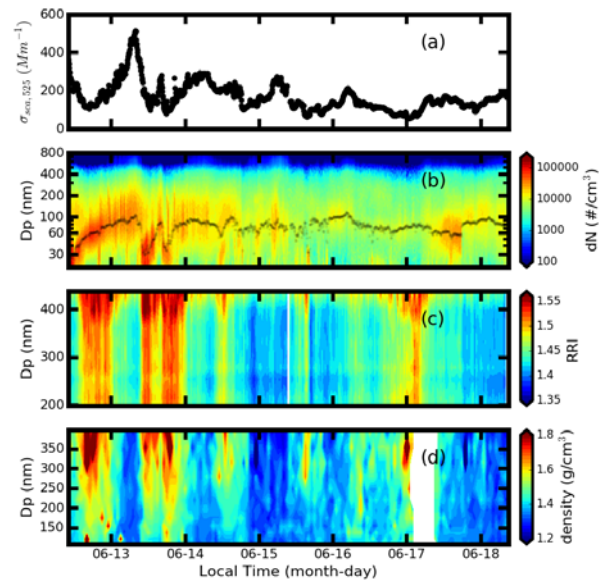
430

431 **Figure 1:** Measurement site of Taizhou (marked with stars). Filled colors represent (a) the  
432 topography of the Jianghuai Plain. (b) the average aerosol optical depth at 550nm during the year of  
433 2017 from Moderate Resolution Imaging Spectroradiometer onboard satellite Aqua.

434

435

436



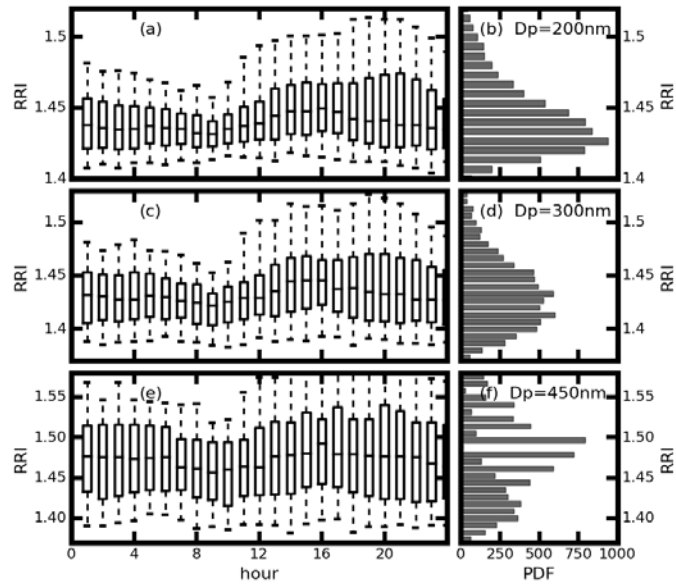
437

438

439

440

**Figure 2.** Time series of the measured (a) size-resolved RRI in filled color,  $\sigma_{sca}$  at 525nm in black dotted line and (b) the size-resolved  $\rho_{eff}$ .



441

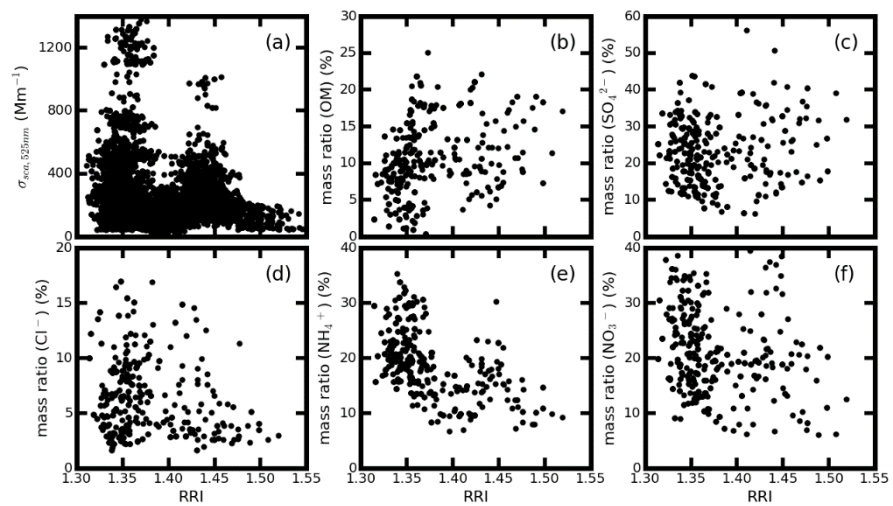
442

443

444

445

**Figure 3.** Daily variations of the RRI (a), (c) (e), and the probability distribution of the measured RRI (b), (d) (f) for the (a), (b) 200 nm, (c), (d) 300 nm, and (e), (f) 450nm aerosol respectively. The box and whisker plots represent the 5<sup>th</sup>, 25<sup>th</sup>, 75<sup>th</sup> and 95<sup>th</sup> percentiles.



446

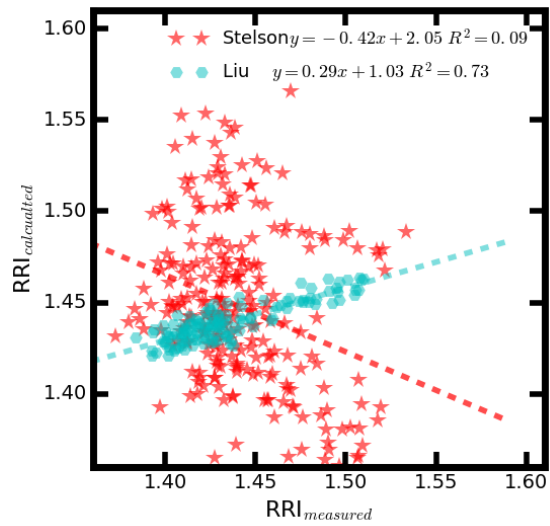
447

**Figure 4.** Comparison the measured RRI at 300nm with the measured (a)  $\sigma_{\text{sca}}$  at 525nm, mass

448

fraction of (b) OM, (c)  $\text{SO}_4^{2-}$ , (d)  $\text{Cl}^-$ , (e)  $\text{NH}_4^+$  and (f)  $\text{NO}_3^-$ .

449

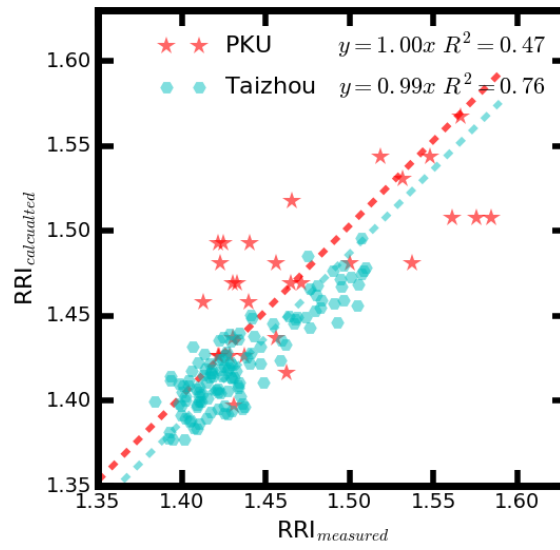


450

451 **Figure 5.** Comparison between the measured RRI and calculated RRI using the main aerosol  
452 chemical component from Stelson (1990) (in red star) and parameterization scheme proposed by Liu  
453 and Daum (2008) (in cyan hexagon).

454

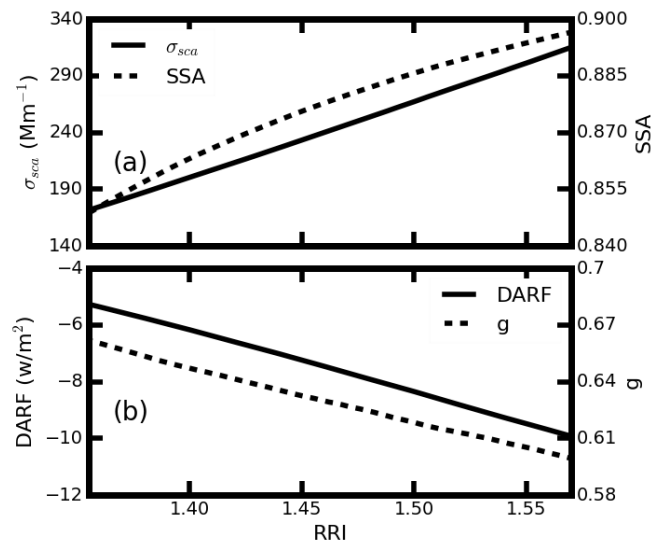
455



456

457 **Figure 6.** Comparison between the measured and calculated RRI for different at PKU (in red star)

458 and Taizhou (in cyan hexagon) station.



460

461

**Figure 7.** Variations of the estimated (a)  $\sigma_{sca}$  in solid line, SSA in dotted line, (b)  $g$  in dotted line,

462

and DARF in solid line for different aerosol RRI.

463